# Analysis and design of a permanent magnet linear synchronous motor based on inductance calculation

ENES YUCEL<sup>1</sup>\*®, MÜMTAZ MUTLUER<sup>2</sup>®, MEHMET ÇUNKAŞ<sup>1</sup>®

<sup>1</sup>Faculty of Technology, Department of Electrical and Electronics Engineering, Selçuk University
Turkey

<sup>2</sup>Faculty of Engineering, Department of Electrical and Electronics Engineering
Konya Technical University
Turkey

e-mail: {\*enes.yucel/mcunkas}@selcuk.edu.tr, mmutluer@ktun.edu.tr

**Abstract:** This paper presents a comprehensive design and analysis methodology for a Permanent Magnet Linear Synchronous Motor (PMLSM), with a focus on evaluating different inductance modeling approaches. The motor design begins with analytical dimensioning based on defined design parameters. A two-dimensional finite element analysis follows this in ANSYS Maxwell to verify magnetic saturation, back-EMF, flux linkage, and electromagnetic performance under full load conditions. The inductance parameters are calculated using both conventional and look-up table (LUT) based models. In the conventional model, seven different methods are tested under static and dynamic conditions, as well as in nonsalient and salient scenarios, and their results are compared. In the LUT model, currentdependent inductance values are extracted from flux linkage maps. The motor designed in Maxwell, along with the calculated inductance data, is integrated into a dynamic cooperative simulation (co-sim) model controlled by an inverter in Simplorer to analyze the thrust force. The results show that the LUT model provides outputs that are closer to the co-sim reference than the traditional model. Furthermore, performance curves based on the Maximum Torque Per Ampere strategy are generated, and the force-speed and power-speed characteristics derived from both inductance models are compared. The findings emphasize the importance of accurate inductance modeling in capturing the actual electromagnetic behaviour of PMLSM under dynamic operating conditions.

**Key words:** cooperative simulation, *d-q* inductance calculation, finite element analysis (FEA), park's transformation, permanent magnet linear synchronous motor (PMLSM)

#### 1. Introduction

Permanent Magnet Linear Synchronous Motors (PMLSMs) have attracted significant interest in both academic and industrial fields due to their high efficiency, direct drive capability, and suitability for precision motion applications such as transportation, automation, and magnetic

launch systems. However, designing these motors requires meeting strict requirements regarding response time, thermal performance, and compactness [1]. In the preliminary design of PMLSMs, magnetic equivalent circuit models are widely used to represent magnetic behaviour, including saturation and harmonics, with sufficient accuracy [2].

Numerous studies have focused on double-sided Permanent Magnet Linear Synchronous Motors (DS-PMLSMs) due to their suitability for high-acceleration applications, particularly in systems where high thrust density and dynamic response are critical. In railway applications, researchers continue to conduct comparative analyses of single- and double-sided PMLSMs while seeking configurations that maximize efficiency and performance under constrained mass and space requirements. Wu and Lu [3] analyzed the current-dependent armature inductance and evaluated the performance of a water-cooled DS-PMLSM driven by a servo system employing Space Vector Pulse Width Modulation (SVPWM) under various operating conditions. Kim *et al.* [4] proposed a dual-line, double-sided vertical structure providing similar thrust to two single-line models while enhancing the thrust-to-weight ratio. Additionally, García-Tabarés *et al.* [5] analyzed different motor types for Hyperloop propulsion. While PMLSMs offer high efficiency and controllability, they also have disadvantages such as cogging force, thrust ripple, and dependence on numerous magnets. To address these issues, optimization of end effects and the adoption of alternative synchronous motor topologies have been proposed.

One of the most critical aspects in modeling, control, and optimization of these motors is the accurate determination of direct-axis (*d*-axis) and quadrature-axis (*q*-axis) inductances. Various methods have been developed to analyze the nonlinear and position-dependent behaviour of inductance in PMLSMs. Ma *et al.* [6] proposed a method to calculate the uncertainty range of *d*-*q* axis inductances using both finite element analysis (FEA) and multi-loop analysis. This approach provides a more realistic understanding of variability under operating conditions. Li *et al.* [7] investigated mutual and self-inductance behaviours in three-phase windings and validated inductance measurement techniques by comparing them with FEA results. Zhang *et al.* [8], in the context of a single-phase PM linear actuator, used eight-node hexahedral elements in FEA and verified the accuracy of inductance and flux linkage calculations through experimental comparison.

Furthermore, Shin *et al.* [9] used a subdomain analytical model offering simplified calculations for end inductances, predicting the armature reaction field and validating the results with 3D FEA and experimental data. Cheng *et al.* [10] examined inductance characteristics in combined iron-core PMLSMs and developed a linear thrust model based on lumped parameters to reduce thrust ripple and improve control. Shi *et al.* [11] studied air-core PMLSMs for null-flux electromagnetic suspension vehicles and evaluated the effects of vertical offsets on thrust performance using dynamic tests and an analytical model based on virtual displacement. Lee *et al.* [12] proposed a fast and efficient analytical field projection method combined with a coil separation technique to determine winding inductance without the need for comprehensive FEA. Similarly, Chang *at al.* [13] reviewed inductance calculation methods and proposed an improved FE-based approach that uses the same field solutions as torque calculations, eliminating the need for additional simulations; the method was validated on a 30 hp PMSM under various load

conditions. The Fixed Permeability Method (FPM) has been used to investigate air gap flux density and cross-coupling effects in Interior Permanent Magnet Synchronous Motors (IPMSMs), yielding high accuracy under magnetic saturation conditions when compared with experimental and FEA model results [14]. According to Lee *et al.* [15], calculating inductance is critical for designing a Flux-Concentrating Permanent Magnet Synchronous Motor (FCPMSM). To address this, a *d-q* axis magnetic equivalent circuit was developed, considering the rotor's nonlinear relative permeability, and validated through FEA.

Wang et al. [16] tackled modeling challenges caused by structural asymmetry in low-speed PMLSMs by developing a nonlinear state-space model and examined the effect of air gap variation on inductance using both FEA and experimental data. Additionally, they proposed a nonlinear, asymmetric, and variable-parameter state-space model for PMLSMs requiring parameters such as self-inductance, mutual inductance, and flux linkage [17]. Zhang et al. [18] further explored the impact of different slot/pole number combinations and winding structures on the electromagnetic behavior of AL-PMSMs, revealing that such design variations substantially influence saturation and flux distribution. Inspired by the segmented PM pole configuration explored in [19], this study investigates the impact of pole structure on inductance characteristics and overall thrust behavior. Xu et al. [20] also investigated the role of phase number and consequent-pole configuration in five-phase PMSLMs, highlighting their influence on inductance behavior. Moreover, Sun et al. [21] examined the variation in d- and q-axis inductances in DTP-PMLSMs and its impact on the accuracy of sensorless control, emphasizing the critical role of parameter sensitivity. Lastly, Zhang and team [22] presented a comprehensive framework for estimating leakage inductance in high-speed double-sided linear synchronous motors, accounting for factors such as slotting, harmonic components, end winding geometry, and tooth tips.

Although various methods have been proposed in the literature to characterize the inductance of PMLSMs, comparative studies that incorporate different saliency conditions and evaluate force generation under full-load conditions are still limited. Moreover, there is a need for comprehensive approaches that assess the impact of constant and variable inductance models on the dynamic behavior of these motors. In particular, studies addressing the effects of different saliency conditions under full-load operation remain limited.

To respond to these gaps, this study systematically analyzes the influence of various inductance modeling strategies on force generation during the PMLSM design process. The proposed methodology begins with a rigorous preliminary design procedure, combining analytical calculations with 2D FEA simulations in ANSYS Maxwell to evaluate electromagnetic and performance parameters under magnetic loading, no-load, and full-load conditions. Subsequently,  $L_a$  and  $L_q$  inductance values are obtained under salient and non-salient conditions using both conventional and look-up table (LUT) based models. These values are then integrated into an inverter controlled cooperative simulation (co-sim) model to analyze the dynamic force output.

The main contribution of this study is that it bridges the gap between d-q axis inductance modeling and dynamic performance evaluation. The results demonstrate not only the accuracy

of the modeling approaches but also their practical applicability for drive systems, highlighting the critical role of inductance parameterization in ensuring reliable force generation.

# 2. Materials and methods

It is possible to control a linear motor in the same manner as a rotary motor by supplying sinusoidal three-phase current to each coil [23]. The surface-mounted PMLSM developed in this study demonstrates behaviour analogous to that of conventional rotary type Permanent Magnet Synchronous Motor (PMSM). The proposed methodology is summarized in the flowchart shown in Fig. 1.

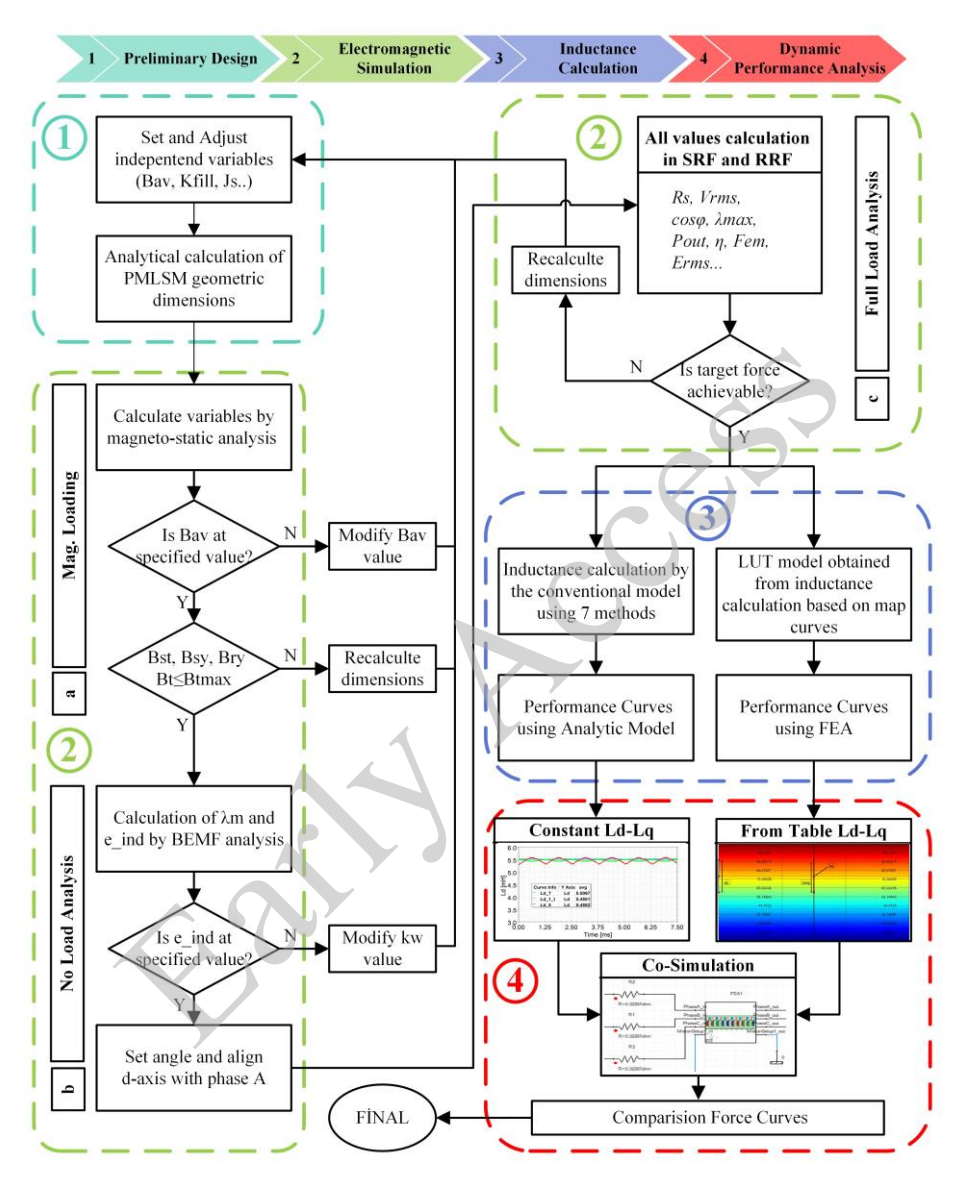


Fig. 1. Flowchart of the proposed PMLSM design process incorporating inductance modeling approaches

The parameters of the PMLSM are first calculated analytically [24]. After the initial decisions on motor dimensions are made, magnetic field analyses are performed using 2D FEA model. Then, the performance analysis is conducted using data obtained through both conventional and LUT based inductance calculation approaches.

This paper has been accepted for publication in the AEE journal. This is the version, which has not been fully edited and content may change prior to final publication.

Citation information: DOI 10.24425/aee.2025.154996

## 2.1. Preliminary design and coordinate transformation

In the preliminary design stage of the motor, no dimensional constraints were imposed other than the stator width  $(L_{stk})$ . The main objective of the design is to achieve the required thrust and efficiency while operating within the voltage limits of the available power source and avoiding magnetic saturation in the core materials. The key design parameters considered during the initial dimensioning of the PMLSM are summarized in Table 1. Using the input power (P<sub>in</sub>), motor speed  $(\vartheta)$ , efficiency  $(\eta_d)$ , output power  $(P_{\text{out}})$  and thrust force  $(F_{\text{out}})$  the analytical equations used for motor sizing are also provided. [25] [26].

$$P_{\text{out}} = F_{\text{out}}\vartheta,\tag{1}$$

$$P_{\rm in} = P_{\rm out}/\eta_d. \tag{2}$$

Given the phase voltage  $(V_{ph})$  and power factor  $(\cos \phi)$ , the phase current is defined:

$$I_{ph} = \frac{P_{\text{in}}}{3V_{ph}\cos\phi}.$$
 (3)

Since back-EMF ratio  $(\gamma_{\rm emf})$  and  $V_{ph}$  are known initially, back-EMF per phase  $(E_{ph})$  can be calculated using the following expression

$$\gamma_{\rm emf} = E_{ph}/V_{ph}. \tag{4}$$

The total flux  $(\varphi_{total})$  is divided by the number of slots  $(N_s)$  and poles (p) to find the flux per slot and per pole:

$$\varphi_{st} = \varphi_{\text{total}}/N_s, \qquad (5)$$

$$\varphi_p = \varphi_{\text{total}}/p. \qquad (6)$$

$$\varphi_p = \varphi_{\text{total}}/p. \tag{6}$$

The stator tooth area  $(A_{st})$  is obtained by dividing the flux through that tooth by the allowable maximum flux density ( $B_{st,max}$ ):

$$A_{st} = \varphi_{st}/B_{st,\text{max}}. (7)$$

Assuming the stator length  $(L_s)$  is known, the slot width  $(w_{ss})$  can be determined by subtracting the total tooth area  $(A_{st})$  from the stator area.

$$w_{ss} = \frac{L_s L_{stk} - N_s A_{st}}{N_s L_s}. (8)$$

The induced phase voltage is the product of the flux linkage ( $\lambda$ ) and electrical angular speed  $(\omega_e)$ . Also, the flux linkage depends on the winding factor  $(k_w)$ , number of turns  $(N_{tph})$ , frequency (f) and flux per pole  $(\varphi_n)$ :

$$E_{nh} = \lambda \cdot j\omega_e, \tag{9}$$

$$\lambda = k_w N_{tvh} \varphi_v. \tag{10}$$

The required number of turns per phase  $(N_{tph})$  is calculated based on the target EMF:

This paper has been accepted for publication in the AEE journal. This is the version, which has not been fully edited and content may change prior to final publication.

Citation information: DOI 10.24425/aee.2025.154996

$$N_{tph} = \frac{E_{ph}}{\sqrt{2\pi f \varphi_n k_w}}. (11)$$

The conductor cross-sectional area is the ratio of the carried current  $(A_w)$  to the selected current density  $(J_s)$ :

$$A_w = \frac{I_s}{I_s}. (12)$$

The area of a single coil side in the slot  $(A_{ca})$  is calculated using the winding fill factor  $(k_{fill})$ and number of turns per coil  $(N_{tc})$ . Since a double-layer concentric winding is used in this study, there are two coil sides per slot, and the total slot area  $(A_s)$  is:

$$A_{ca} = (N_{tc}A_w)/k_{fill}, (13)$$

$$A_s = 2A_{ca}. (14)$$

The height of the coil is calculated based on the placement area of the coil sides in the slot and the coil width  $(w_c)$ :

$$d_c = A_{ca}/w_c. (15)$$

The stator yoke  $(h_{sy})$  and rotor yoke height  $(h_{ry})$  are calculated based on the maximum flux density in the stator yoke  $(B_{sy,max})$  and rotor yoke  $(B_{ry,max})$ :

$$\frac{\varphi_{st}}{2} = B_{sy,\max} h_{sy} L_{stk},\tag{16}$$

$$\frac{\varphi_{st}}{2} = B_{sy,\text{max}} h_{sy} L_{stk}, \tag{16}$$

$$\frac{\varphi_p}{2} = B_{ry,\text{max}} h_{ry} L_{stk}. \tag{17}$$

Table 1. Design parameters for the PMLSM

Parameters	Values	Parameters	Values
$F_{ m out}$	570 N	$N_{S}$	12
$P_{ m out}$	3.7 kW	р	16
θ	6.55 m/s	$L_{stk}$	80 mm
$V_{ph}$	121 V	$J_s$	4 A/mm <sup>2</sup>
η	90%	$L_{ m gap}$	1 mm
$B_{av}$	0.68 T	$B_{st,\max}$	1.80 T
Core material	M19-24G	$B_{sy,\max}$	1.50 T
Magnet grade	N38-20C	$B_{ry,\max}$	1.50 T

Due to their structural characteristics, PMLSMs exhibit nonlinear and strongly coupled electromagnetic behaviour. To simplify this coupling and enable effective control, using the Clarke–Park transformations are applied from the three-phase a-b-c system (ABC) to the stationary  $\alpha$ - $\beta$  reference frame (SRF), and subsequently to the synchronous rotating d-q reference frame (RRF). When modeling in the d-q frame, assuming the d-axis current ( $i_q$ ) to be zero enables thrust force control solely through the q-axis current ( $i_q$ ). This assumption not only simplifies the mathematical representation of the system but also facilitates direct control over thrust production.

In this study, the d-q reference frame was used to model the electromagnetic behaviour of PMLSM. This transformation plays an effective role in both establishing the force equations during the design stage and interpreting the results from FEA model [27].

### 2.2. Electromagnetic simulations

Following the initial analytical sizing, magnetostatic and transient analyses based on 2D FEA were conducted to investigate the electromagnetic behaviour of the motor. The methodology used in this study involves four simulation runs over electrical periods. The solver types and simulation parameters employed in each analysis are summarized in Table 2.

The primary objective of the initial magnetic loading analysis was to evaluate the air-gap magnetic flux density  $(B_{av})$  generated by the permanent magnets. If insufficient, it may hinder achieving the desired force in steady-state analysis. Figure 2 illustrates the flux density distribution and flux lines, showing mutual flux paths and limited leakage. The values corresponding to  $m_1$ ,  $m_2$ , and  $m_3$  at critical points are presented in the table as 1.698 T for the stator yoke  $(B_{sy})$ , 1.279 T for the rotor yoke  $(B_{ry})$ , and 1.31 T for the stator tooth  $(B_{st})$ , respectively, indicating magnetic saturation.

Parameter	Mag. loading	No-load	Full load	Dynamic load				
Solver type	Magneto-static	Transient	Transient	Transient-simplorer				
Excitation	None	None	Current	Variable load				
Rotor motion	No	Yes	Yes	Yes				
Stop time	_	Те	Те	Application specific				
Time step	_	Te/400	Te/400	Adaptive				

Table 2. Solver types and simulation parameters used in 2D FEA

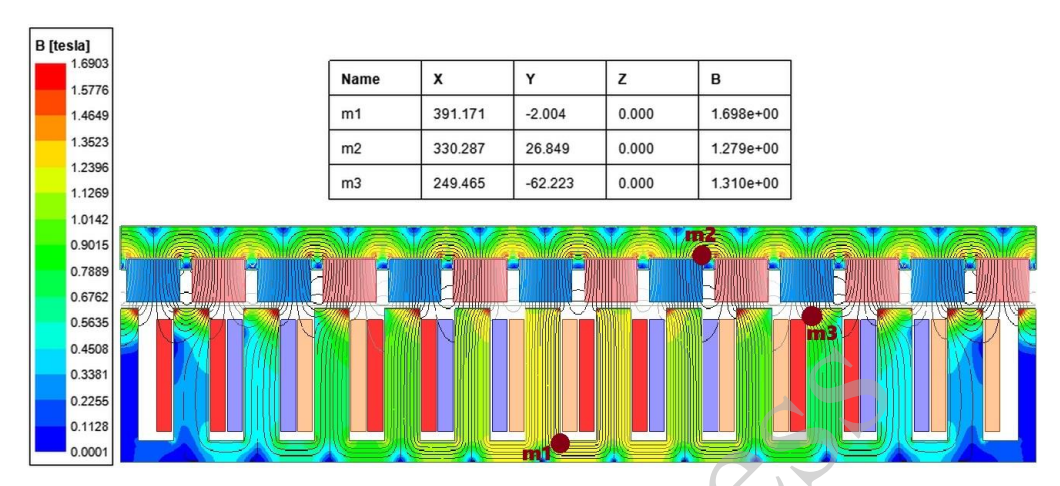
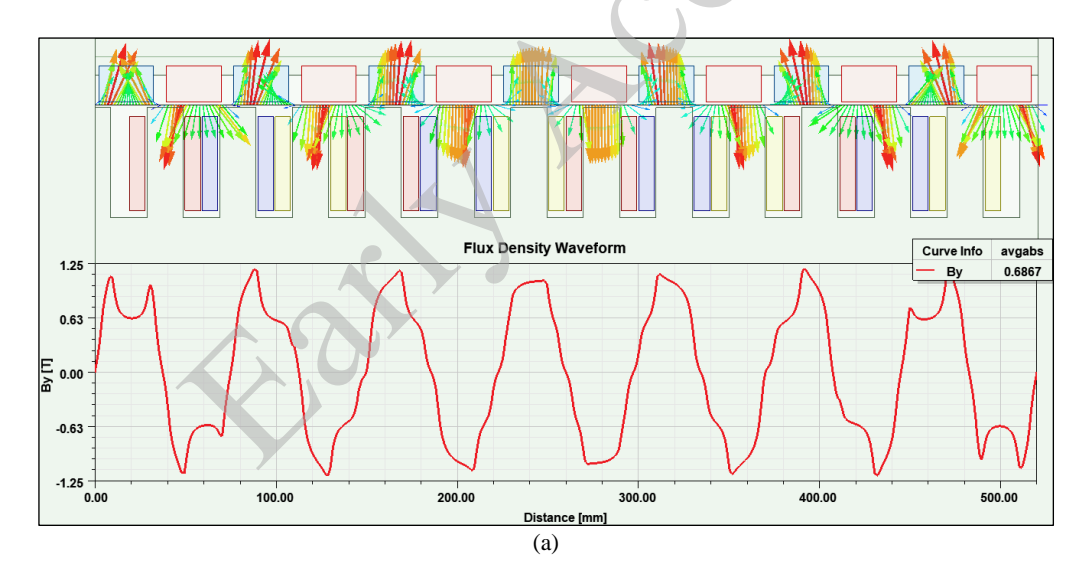


Fig. 2. Flux lines and flux density magnitude from magnetic loading simulation

The results of the magnetic loading analysis are presented in Fig. 3.



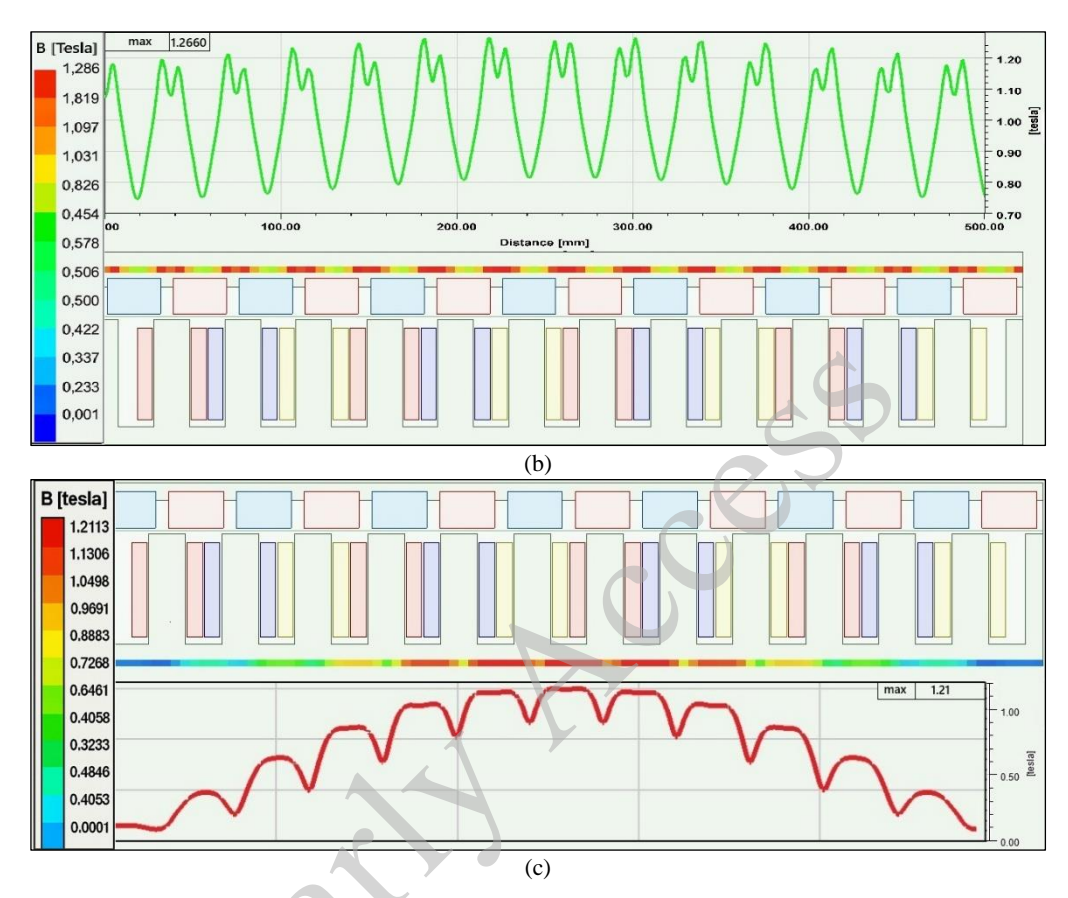


Fig. 3. The level of saturation, vector lines and flux density waveforms obtained from magnetic loading simulation: air gap (a); rotor yoke (b); stator yoke (c)

In Fig. 3(a), the waveform of the magnetic flux density component along the air gap is shown together with vector field lines, and  $B_{av}$  is calculated to be approximately 0.687 T. Figures 3(b) and 3(c) present the flux density profiles and indicate the saturation behaviour on candidate paths. In all three figures, the waveform of the magnetic flux density and the vector field lines exhibit a periodic structure that matches the magnet arrangement and the colour distribution. The maximum values reached along the candidate path are 1.266 T in the rotor yoke and 1.21 T in the stator yoke. As is seen in Figs. 2 and 3, the flux density levels in the iron parts remain below the design limits set for  $B_{st,max}$ ,  $B_{sy,max}$  and  $B_{ry,max}$  confirming that the saturation levels are acceptable.

After the magnetic loading analysis, a no-load analysis is performed, in which no excitation is applied to the stator windings, and the rotor moves at a constant speed under the magnetic field generated solely by the permanent magnets. The  $k_w$  was updated using an iterative approach to achieve the  $E_{ph}$  value. As shown in Fig. 4(a), the maximum flux linkage ( $\lambda_{max}$ )

value of 0.175 Wb observed in each phase also represents the magnet-induced flux linkage component ( $\lambda_M$ ). In Fig. 4(b), the rms value of the induced voltage is calculated to be approximately 102.9 V. According to the figures, the sinusoidal waveforms obtained for each phase are symmetric with a 120° phase difference. This indicates that the magnets provide a uniform magnetic field distribution across the air gap, resulting in minimal harmonic content, which in turn positively affects the motor's performance.

As shown in the schematic view in Fig. 5, the d-axis flux linkage value ( $\lambda_d$ ) originates from the permanent magnets. The q-axis is perpendicular to the d-axis. In motor control, phase A is typically used as the reference phase; accordingly, the phase A winding axis is aligned with the stator's  $\alpha$ -axis [28, 29]. The angle  $\omega_e$  represents the electrical angle between the d-axis and the A phase winding axis. If the rotor's d-axis does not coincide with the phase A winding axis when  $\omega_e t = 0$ , then the initial alignment angle is incorrect. Therefore, we must make sure that the d-axis is aligned with the centre of the phase. The angle between the current vector and the stator  $\alpha$ -axis ( $\theta_s$ ) is equal to the sum of the angle between the current vector and the rotor's d-axis ( $\theta_r$ ) and  $\omega_e t$ . To achieve proper alignment, a constant alignment angle ( $\theta_0$ ) is introduced as shown in Eq. (18), and this adjustment is implemented within the FEA software.

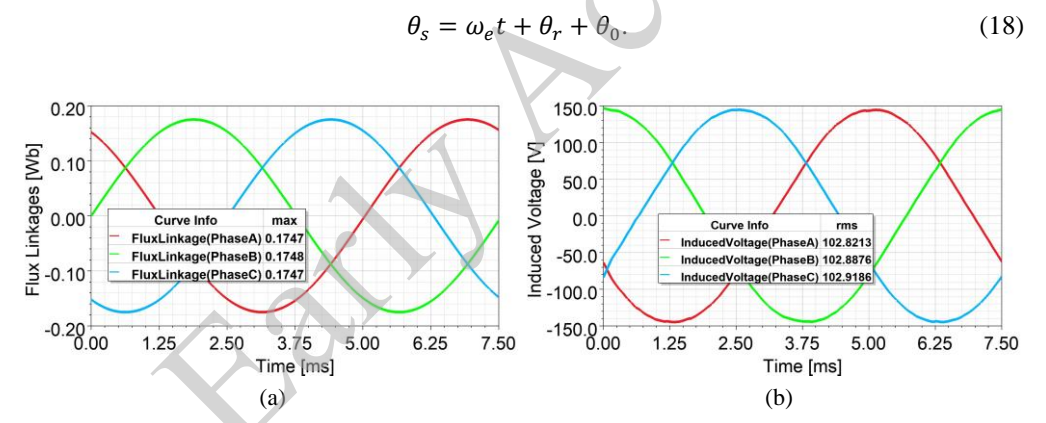


Fig. 4. No-load simulation results: flux linkage waveforms (a); induced voltage waveforms (b)

Accordingly, the analysis performed to determine the value of  $\theta_0$  indicates that the maximum flux linkage of phase A, as shown in Fig. 6, is approximately 0.17 Wb. The electrical angle value at which this maximum point occurs is the angle at which the magnet is fully aligned with the phase A winding. Hence, the electrical angle at this point 331.27° is taken as the value of  $\theta_0$ . Since this angle is behind the *d*-axis relative to the phase A axis, it is taken as negative. This means that the axis is shifted by 28.73°.

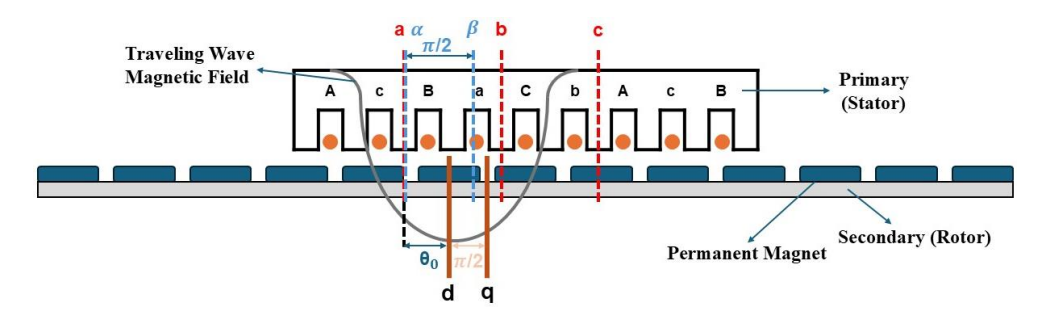


Fig. 5. Schematic view of the studied PMLSM

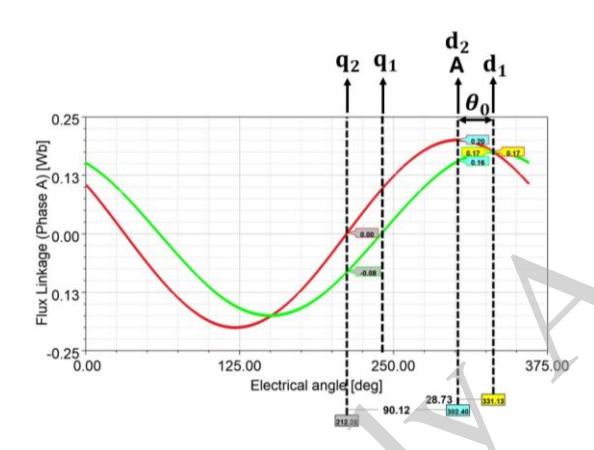


Fig. 6. Phase A flux linkage waveform for identifying  $\theta_0$ 

In the final stage of the electromagnetic simulations, the parameters listed in Table 1 were implemented in the simulation environment, and the electromagnetic performance of the PMLSM under full-load operating conditions was comprehensively analyzed. Then final geometrical parameters and output variables were calculated.

In the analysis of PMLSMs, mathematical modeling is carried out in the d-q synchronously rotating reference frame [30]. Accordingly, the dynamic equivalent circuits for the d-q axes are defined, and the corresponding voltage equations are given as follows. Here,  $V_d$  and  $V_q$  are the voltages,  $i_d$  and  $i_q$  are the currents, and  $L_d$  and  $L_q$  are the inductances in the respective axes:

A pole pitch  $(\tau)$ , which is the distance between two consecutive magnetic poles:

$$\tau = \frac{\vartheta}{2f}.\tag{19}$$

Accordingly, the electrical angular velocity ( $\omega_e$ ) of the PMLSM can be expressed as:

$$\omega_e = \frac{\pi * \vartheta}{\tau},\tag{20}$$

$$V_d = R_s i_d + L_d \frac{\mathrm{d}i_d}{\mathrm{d}t} - \frac{\pi}{\tau} \vartheta L_q i_q, \tag{21}$$

$$V_q = R_s i_q + L_q \frac{\mathrm{d}i_q}{\mathrm{d}t} + (L_d i_d + \lambda_M) \frac{\pi}{\tau} \vartheta. \tag{22}$$

Maximum force is achieved under the condition where the q-axis current component vector is perpendicular to the magnet flux linkage ( $\lambda_M$ ) vector ( $\theta_r = 90^\circ$ ). The electromagnetic thrust force is calculated using:

$$F_{em} = \frac{3\pi}{2\tau} \left[ \lambda_M + \left( L_d - L_q \right) i_d \right] i_q. \tag{23}$$

The force in Fig. 7(a) is close to the 570 N target, confirming  $\theta_0$  and  $\theta_r$  alignment parameters validity with good FEA and analytical agreement. As seen in Fig. 7(b), the maximum force occurs at  $\theta_r = 90^{\circ}$  consistent with theory. Final geometry and outputs are listed in Table 3, with simulation results summarized in Table 4. As seen in Fig. 7(b), the maximum force occurs at  $\theta_r = 90^{\circ}$  consistent with theory. Final geometry and outputs are listed in Table 3, with simulation results summarized in Table 4.

Geometrical parameters			Output variables				
Parameter definition	Symbol	Value	Parameter definition	Symbol	l Value		
Slots number	$N_s$	12	Yoke flux (tesla)	Ву	1.28		
Pole number	p	16	Tooth flux density (tesla)	$B_t$	1.69		
Stator width (mm)	Lstk	80	Total motor mass (kg)	m	26.3		
Stator length (mm)	$L_s$	396	Motor speed (m/s)	θ	6.55		
Stator height (mm)	$H_s$	73.25	Frequency (Hz)	f	132		
Slot width (mm)	$w_s$	13	Thrust force (N)	$F_{em}$	565.6		
Slot depth (mm)	$h_s$	53.25	Output power (W)	$P_{ m out}$	3705		
Tooth width (mm)	$W_t$	20	Copper loss (W)	$P_{cu}$	139		
Stator yoke (mm)	hsy	20	Solid loss (W)	$P_{ m solid}$	113		
Rotor yoke (mm)	hry	15	Core loss (W)	$P_{\rm core}$	346		
Air gap length (mm)	$L_{gap}$	1	Phase resistance (Ω)	$R_s$	0.323		
Magnet width (mm)	$W_m$	30	Power factor	$\cos \varphi$	0.895		
Magnet height (mm)	$h_m$	20	Stator RMS current (A)	$I_p$	12		
Magnet depth (mm)	$d_m$	80	Number of turns per slot	$N_{tc}$	45		
Magnet spacing (mm)	$b_m$	7	Number of turns per phase	$N_{tph}$	180		

This paper has been accepted for publication in the AEE journal. This is the version, which has not been fully edited and content may change prior to final publication.

Citation information: DOI 10.24425/aee.2025.154996

Conductor area (mm²)	$A_{\scriptscriptstyle W}$	330	Wire cross section (mm²)	$A_w$	3
Pole pitch (mm)	τ	24.75	Current density (A/mm²)	$J_s$	4
Slot pitch (mm)	Λ	33	Efficiency	η	%91.7

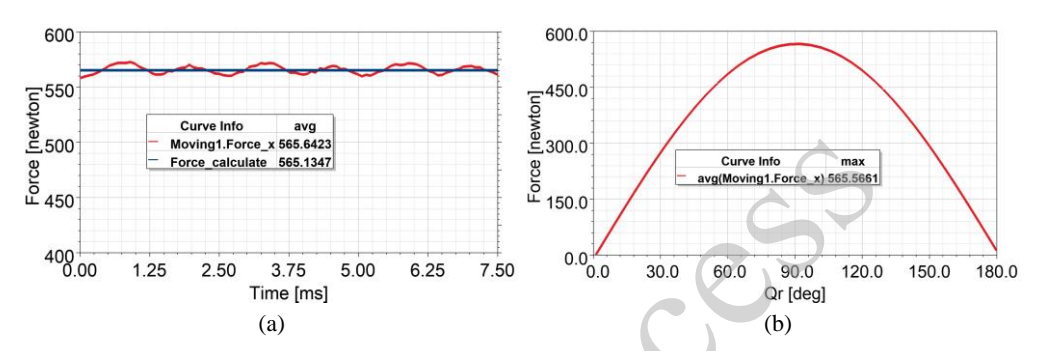


Fig. 7. Analyzed and calculated force curve (a); static force curve (b)

Table 4. PMLSM output parameters under full load 2D FEA in ABC, SRF and RRF

Outsuit is it has	Ch al	ABC	SRF		RRF	
Output variables	Symbol	a, b, c	α	β	d	q
Induced voltage (V)	$E_{ m rms}$	117.58	117.58	117.70	-76.32	147.83
Flux linkage (Wb)	$\lambda_{ m max}$	0.20	0.20	0.20	0.175	0.097
Current (A)	$I_{ m max}$	16.97	16.97	19.97	0	16.97
Phase voltage (V)	$V_{ m rms}$	121.04	121.04	121.04	-76.32	153.31

# 2.3. Calculation of Inductances in the d and q axes

Inductance characterizes a coil's ability to store and release magnetic energy. In this study, the idealized synchronous machine model assumes a constant and a position-dependent air gap permeance component to reflect saliency and the  $L_d-L_q$  difference. Additionally, only the fundamental component of the air-gap flux is considered, neglecting spatial harmonics to simplify inductance calculations [31]. In this study, two inductance modeling approaches were used: a conventional model and a LUT model derived from flux linkage maps. The conventional model examined seven inductance calculation methods, using the results as constant  $L_d$  and  $L_q$  values. In contrast, the LUT model used current-dependent inductance data structured as tables. The methods in the conventional model are systematically classified in Table 5 and were performed using a magneto-static solver for time-dependent/stationary conditions and a transient solver for current-dependent/moving conditions.

The values presented in Table 6 were obtained as inductance results for conventional model methods under different conditions. In the static condition, magnets are modeled as vacuum to exclude their effect, while dynamic simulations include them. To eliminate geometric influences, the secondary surface is symmetrized, referred to as the non-saliency condition, while the normal saliency condition includes this asymmetrical. The table, which also includes magnetic energy  $(W_{\varphi})$ , magnetizing inductance  $(L_m)$ , and mutual inductance  $(L_{mn})$ . To calculate the  $L_d$  value, the rotor electrical angle  $\theta_r$  must be set to zero. As seen in Fig. 10(e), the q-axis flux linkage  $(\lambda_q)$  is zero, while the d-axis flux linkage  $(\lambda_d)$  increases linearly. To calculate the  $L_q$  value,  $\theta_r$  must be set to 90°. As shown in Fig. 10(f), in the dynamic simulation with magnets included,  $\lambda_d = \lambda_M$ , while  $\lambda_q$  increases linearly with the  $i_q$  component.

Table 5. Inductance calculation methods for the conventional model

No	Method	Definition	Solver type	Model
1-m	Linear inductance	$L_d = \frac{\lambda_d - \lambda_M}{i_d}$	Magneto-static	
1-t	Linear inductance	$L_q = \frac{\lambda_q}{i_q}$	Transient	Linear
2	Energy	$W_{\varphi} = L \int_{0}^{i} i \mathrm{d}i = \frac{1}{2} L i^{2}$	Magneto-static	Linear
3	Local inductance	$L = \frac{\mathrm{d}\lambda}{\mathrm{d}i}$	Magneto-static	Non- linear
4	Step response	Find Te; $L = R_s \times T_e$ $V = L \frac{di}{dt} + R_s i$ $i(t) = \frac{V}{R} \left( 1 - e^{-\frac{R}{L}t} \right)$ $T_e = \frac{L}{R_s}$ $L = R_s \cdot T_e$	Transient (DC excitation only, no motion)	Non-lin- ear
5	AC signal	$L = R_s \cdot T_e$ $V_d = R_s i_d - \frac{\pi}{\tau} \vartheta L_q i_q$ $Lq = \frac{R_s I_d - V_d}{\omega_e i_q}$ $L_d = \frac{V_q - R_s i_q - \lambda_M \omega_e}{\omega_e i_d}$	Steady state transient (Equivalent circuit solution)	Non-lin- ear
6	Inductance matrix-1	$\lambda_d = \left(L_a - L_{ab} - L_{ac} + 0.25L_b\right)$	Magneto-static	
7	Inductance matrix-2	$+ 0.25L_c + 0.5L_{bc} \times \frac{2}{3} \times i_d + \lambda_M$	Steady state transient	Non-lin- ear

$\lambda_q = \frac{L_b + L_c - L_{bc} - L_{cb}}{2} \times i_q$	

Table 6.  $L_d$  and  $L_q$  results for conventional model methods under different conditions

			L <sub>d</sub> (1	nH)			$L_q$ (mH)				
		Normal	saliency	Non-sa	liency		Normal	saliency	Non-sa	liency	
Method	Symbol	Dynamic	Static	Dynamic	Static	Symbol	Dynamic	Static	Dynamic	Static	
1 m	$L_{d1m}$	5.62	5.62	5.50	5.50	$L_{q1 \text{ m}}$	5.79	5.62	5.67	5.50	
1 t	$L_{d1t}$	5.634	5.615	5.485	5.500	$L_{q1}$ t	5.793	5.623	5.669	5.500	
2.	$L_{d2}$	5.346	5.146	5.245	5.146	$L_{q2}$	5.346	5.146	5.24	5.146	
3.	$L_{d3}$	5.67	5.62	5.49	5.50	$L_{q3}$	5.79	5.62	5.67	5.50	
4.	$L_{d4}$	5.770	5.665	5.552	5.454	$L_{q4}$	5.678	5.694	5.552	5.48	
5.	$L_{d5}$	5.627	5.614	5.485	5.499	$L_{q5}$	5.633	5.622	5.506	5.499	
6.	$L_{d6}$	5.624	5.601	5.507	5.484	$L_{q6}$	5.627	5.607	5.505	5.486	
7.	$L_{d7}$	5.626	5.611	5.506	5.492	$L_{q7}$	5.628	5.611	5.509	5.492	

According to the analysis results, the overall comparison of the methods is presented in Fig. 8. Method 4 demonstrates high sensitivity to magnetic saturation, producing a significant difference in  $L_d$  under normal saliency conditions, whereas the difference in  $L_q$  remains relatively small. This indicates that the method effectively captures the impact of saturation. Additionally, the fact that the  $L_d$  and  $L_q$  differences remain below 0.18 mH for all methods indicates that geometric symmetry is successfully achieved in the no-saliency condition. In the current study, considering that there is a slight saliency for PMLSM, the method that best demonstrates the saliency effect in analyses conducted under normal saliency-dynamic conditions is the 1 m method, which has the highest difference between  $L_q$  and  $L_d$  at 0.17 mH.

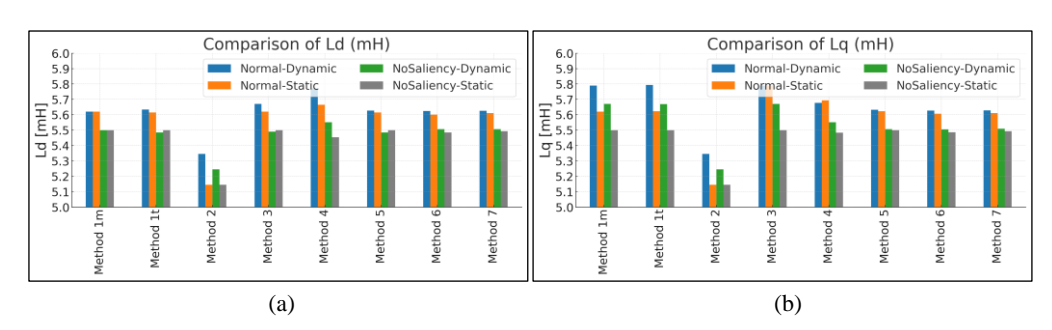


Fig. 8. Comparison of inductance values:  $L_d$  (a);  $L_q$  (b)

In Fig. 9(a), the inductance values are almost equal for almost all methods.

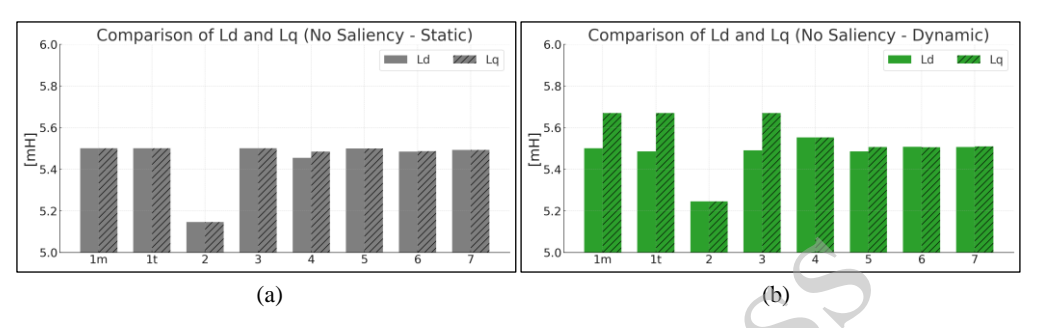
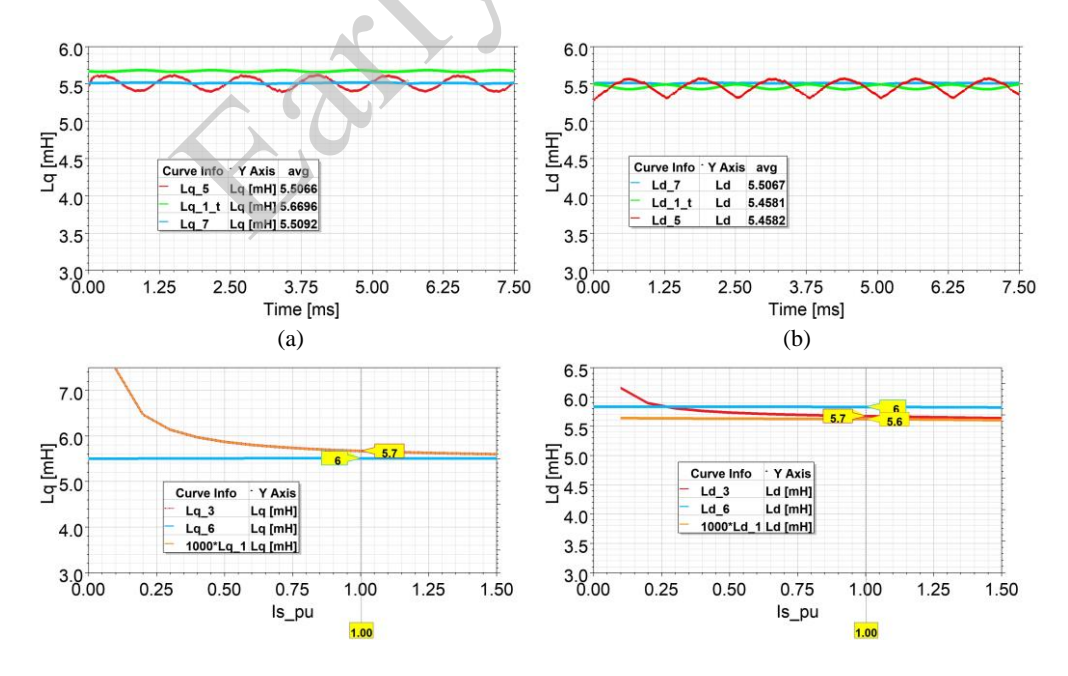


Fig. 9. Comparison of inductances values: non-saliency - static (a); non-saliency - dynamic (b)

This indicates that the methods were correctly implemented in the simulation and that the calculations were performed accurately. As shown in Fig. 9(b), the analyses conducted under dynamic conditions include solutions that include harmonic effects.

Methods 6 and 7, using an inductance matrix, inherently account for harmonics and saturation, resulting in high consistency and low deviation under all conditions. Accordingly, time-dependent average values obtained from the transient solver are shown in Figs. 10(a) and 10(b), while Figs. 10(c) and 10(d) present the results from the magnetostatic solver for  $I_{s-pu}=1$ . These results indicate that the values obtained using different methods are consistent with those from Methods 6 and 7.



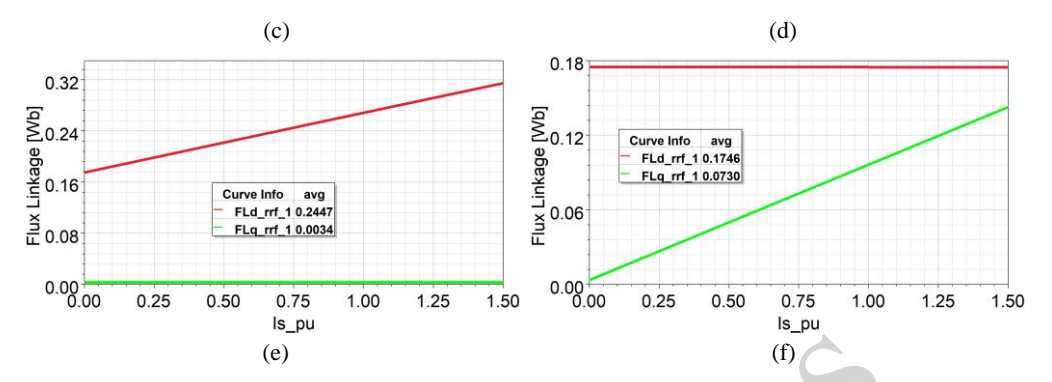


Fig. 10. Results under no saliency, dynamic conditions: time dependent  $L_q$  values for methods 1 t, 5, and 7 (a); time dependent  $L_d$  values for methods 1 t, 5, and 7 (b); current dependent  $L_q$  values for methods 1 m, 3, and 6 (c); current dependent  $L_d$  values for methods 1 m, 3, and 6 (d); current dependent flux linkage at  $\theta_r = 0^\circ$  (e); current dependent flux linkage at  $\theta_r = 90^\circ$  (f)

The second model for obtaining inductance values is the LUT model, derived from flux linkage map curves and excluding cross-magnetization, calculates thrust and flux linkage based on per-unit values of  $i_d$  and  $i_q$ . A current-dependent inductance table is generated from this data. Fig. 11(a) shows that  $\lambda_d$  decreases with more negative  $i_d$ , while Fig. 11(b) shows a linear increase in  $\lambda_q$  with  $i_q$ . In addition, on both map curves, the points and intervals required for calculating local and linear inductances are indicated. Figure 11(c) shows the force contour for the non-salient case, where force varies only with  $i_q$ .

The performance curves were generated using inductance values obtained from two different models. Among the conventional methods, Method 7 was identified as the most suitable option, and the constant inductance values derived from this method were used. In the LUT based model, inductance values were applied as current dependent functions derived from flux linkage maps. In this optimization framework, the resultant voltage  $(V_s)$  of the  $V_d$  and  $V_q$  components are defined as a function of the current components  $i_d$  and  $i_q$ , as shown in Eq. (24).

$$V_s = \sqrt{\left(R_s i_d - \omega_e \lambda_q\right)^2 + \left(R_s i_q + \omega_e \lambda_d\right)^2}.$$
 (24)

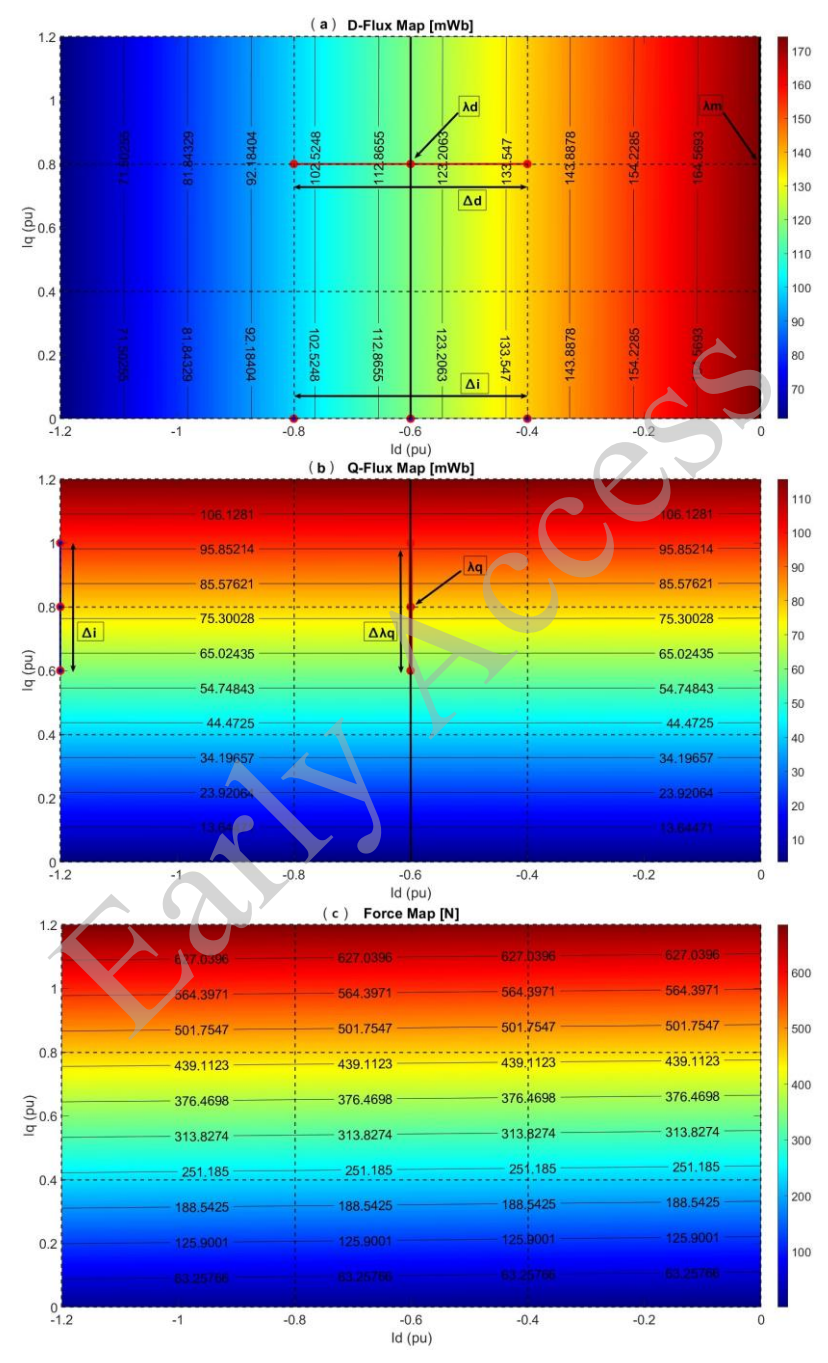


Fig. 11. Map curves: D-Flux Map (a); Q-Flux Map (b); Force Map (c)

This process can be regarded as an optimization method based on the Max Torque Per Ampere (MTPA) strategy. Currents are evaluated at each speed step, and any operating points exceeding the motor's voltage limit are eliminated. The transition to the field weakening region naturally occurs when the system reaches the voltage boundary. This approach enables identification of the optimal operating point that provides maximum thrust force at each speed step along the performance curve. In MTPA-based control, since a negative  $i_d$  current is applied in the field weakening region, map curves corresponding to the second quadrant must be calculated. Figure 12 presents thrust-speed and power-speed performance curves at three current levels for the PMLSM, using inductances from both the LUT and conventional models. Using LUT-based inductances, the curves were calculated through FEA, while those from the conventional model inductances were derived analytically based on an equivalent circuit.

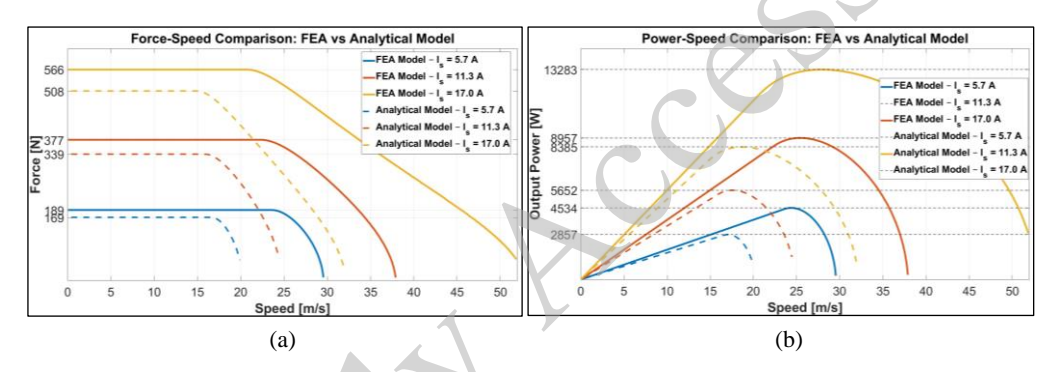


Fig. 12. Performance curves obtained by the FEA model and by the analytical model under different current levels: force-speed curve (a); power-speed curve (b)

In Figure 12(a), the motor operates in the first region, producing maximum and constant force as it has not yet reached the voltage limit. When speed increases and  $V_s$  reaches this limit, the force begins to decrease, marking the transition from the constant force region to the flux weakening region. This breakpoint occurs at lower speeds in the analytical model than in the FEA model. Additionally, the force values from the FEA model are consistent with the target value defined in the initial design. In Fig. 12(b),  $V_s$  increases with speed until the transition to the field weakening region, after which it decreases due to a reduction in power factor at higher speeds.

### 3. Dynamic performance analysis

The objective of the dynamic performance analysis is to comparatively evaluate the impact of different  $L_d$  and  $L_q$  values obtained from the electromagnetic design of the PMLSM on the system's dynamic force output. For this purpose, both the constant inductance values derived from the conventional model and the current dependent inductance data obtained from the LUT

model were employed. Both models were integrated into inverter controlled Simplorer-based dynamic simulations Fig. 13.

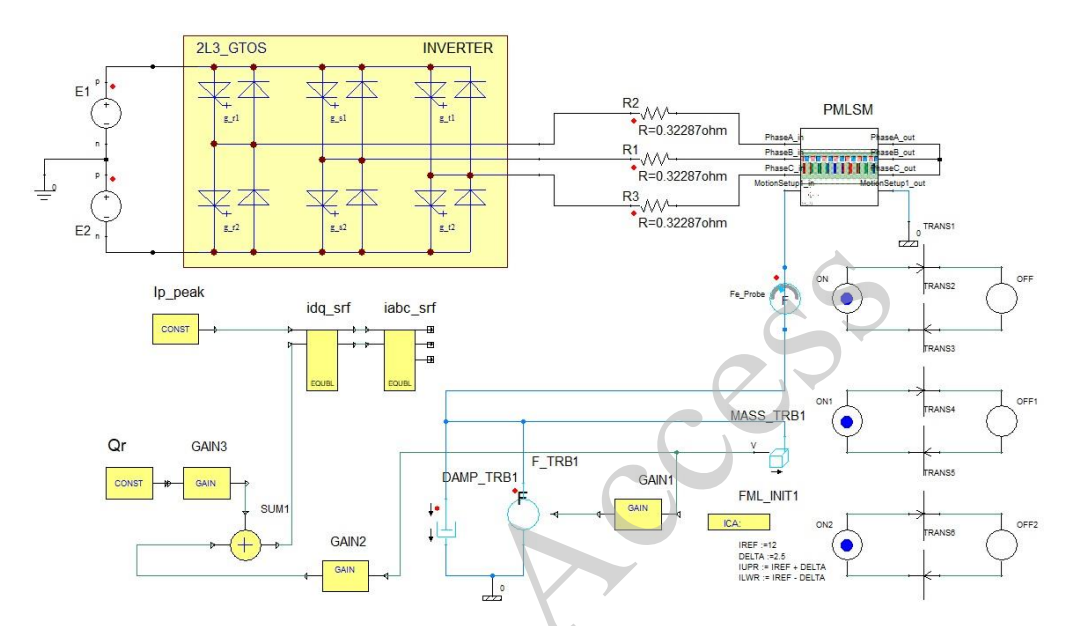


Fig. 13. General view of the dynamic performance simulation

In this study, the resulting force–time responses were compared using a co-sim model, in which the PMLSM, modeled in the electron agnetic analysis software, operates in real time and in coordination with the control model in Simplorer. The dynamic performance analysis was conducted based on the motor's speed and position. As a result, the thrust force-time curves obtained from different modeling approaches were compared, and the system's dynamic behaviour, along with load and friction forces, was analyzed. Thus, the critical role of accurate parameter modeling for force generation has been demonstrated by evaluating the accuracy and practical applicability of inductance modeling approaches in drive systems. Accordingly, the calculated force values are presented in the performance curves shown in Fig. 14.

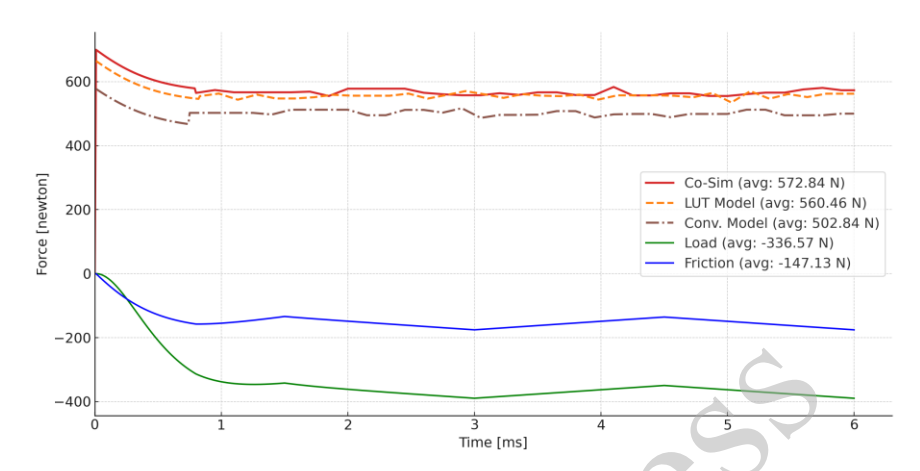


Fig. 14. Thrust force comparison under dynamic load simulation

When comparing the co-sim, LUT model, and conventional model, the average force values were determined to be 572.84 N, 560.46 N, and 502.84 N, respectively. The oscillation characteristics of the models exhibited very similar behaviour. On the other hand, the lower force level observed in the conventional model indicates that this approach does not adequately represent the nonlinear effects in the system. The results show that, when considering the co-sim model as a reference, the LUT based approach yields force values that are closer to it.

# 4. Conclusion

This paper presented a comprehensive design, analysis, and performance evaluation of a surface-mounted PMLSM, with a particular focus on the effects of inductance modeling approaches on dynamic behaviour and thrust generation. Two distinct inductance modeling techniques, conventional and LUT based, were examined under various conditions, including saliency and dynamic operation. Seven different methods within the conventional model were evaluated and classified based on their solver types, input assumptions, and sensitivity to magnetic saturation. The results demonstrated that inductance values obtained using Methods 6 and 7 of the conventional models provided the most consistent and accurate results among the tested techniques. However, due to its ability to incorporate current-dependent variations, the LUT based model more closely represented the system's nonlinear electromagnetic characteristics and produced force values closer to those obtained from the co-sim environment. Performance curves generated under the MTPA strategy further confirmed that the LUT model offers superior predictive capability, especially in capturing the motor's behaviour across different speed ranges. Additionally, dynamic co-sim analysis validated the improved accuracy of the LUT model, particularly under transient operating conditions.

#### Acknowledgements

The authors were supported within the scope of the research by the Selcuk University Scientific Research Projects Coordination (BAP) with Project No: 24111004.

#### References

- [1] Qian J., Zhao C., Pan N., Xie T., *Design and performance analysis of permanent magnet linear synchronous motor*, Journal of Intelligent & Fuzzy Systems, vol. 40, no. 4, pp. 7811–7818 (2021), DOI: 10.3233/JIFS-189602.
- [2] Krämer C., Kugi A., Kemmetmüller W., Modeling of a permanent magnet linear synchronous motor using magnetic equivalent circuits, Mechatronics, vol. 76, 102558 (2021), DOI: 10.1016/j.mechatronics.2021.102558.
- [3] Wu L., Lu Q., Optimal Design and Control Simulation of a High-Accelerate Double-Sided Permanent-Magnet Linear Synchronous Motor, in 2022 25th International Conference on Electrical Machines and Systems (ICEMS), IEEE, pp. 1–6 (2022), DOI: 10.109/ICEMS56177.2022.9982976.
- [4] Kim C.-E., Kim B.-C., Kim M.-S., Design and Analysis of the 2-line Perpendicular Permanent Magnet Double-Sided Linear Synchronous Motor to Increase the Thrust/Weight, in 2022 25th International Conference on Electrical Machines and Systems (ICEMS), IEEE, pp. 1–4 (2022), DOI: 10.1109/ICEMS56177.2022.9983423.
- [5] García-Tabarés L., Lafoz M., Torres J., Soriano G., Orient D., Fons D., Analysis of Alternatives for the Acceleration of a Hyperloop System, in Ibero-American Congress of Smart Cities, Springer, pp. 259–271 (2020), DOI: 10.1007/978-3-030-69136-3\_18.
- [6] Ma M., Xu Z., Zhang X., Tao W., Zhang Y., Wang Z., Dq axis inductance calculation for PMLSM considering end effect and magnetic saturation, in 2021 13th International Symposium on Linear Drives for Industry Applications (LDIA), IEEE, pp. 1–5 (2021), DOI: 10.1109/LDIA49489.2021.9505970.
- [7] Li L., Hong J., Wu H., Kou B., Liu R., *Direct and quadrature inductances measurement of the permanent magnetic linear synchronous machines*, Energy conversion and management, vol. 52, no. 5, pp. 2282–2287 (2011), DOI: 10.1016/j.enconman.2010.12.020.
- [8] Zhang H., Wang Z., Chen M., Shen Z., Yu H., Xu Z., Finite Element Analysis of Electromagnetic Characteristics of a Single-Phase Permanent Magnet Linear Oscillation Actuator, Sensors, vol. 25, no. 2, 452 (2025), DOI: 10.3390/s25020452
- [9] Shin K.-H., Cho H.-W., Lee S.-H., Choi J.-Y., *Armature reaction field and inductance calculations* for a permanent magnet linear synchronous machine based on subdomain model, IEEE Transactions on Magnetics, vol. 53, no. 6, pp. 1–4 (2017), DOI: 10.1109/TMAG.2017.2665661.
- [10] Cheng Y., Yang J., Huang Q., Characteristics of inductance parameters and thrust linear modeling of PMLSM with combinational iron-cored primary, in 2011 International Conference on Consumer Electronics, Communications and Networks (CECNet), IEEE, pp. 142–145 (2011), DOI: 10.1109/CECNET.2011.5768572.
- [11] Shi H. et al., Characteristics Investigation and Dynamic Test of Air-Cored Permanent Magnet Linear Synchronous Motor for null-flux PMEDS Vehicle, IEEE Transactions on Instrumentation and Measurement (2024), DOI: 10.1109/TIM.2024.3406838.
- [12] Lee J.-Y., Hong J., Jang J., Kang D., *Calculation of inductances in permanent magnet type transverse flux linear motor*, International Journal of Applied Electromagnetics and Mechanics, vol. 20, no. 3–4, pp. 117–124 (2004), DOI: 10.3233/JAE-2004-655.
- [13] Chang L., An improved FE inductance calculation for electrical machines, IEEE Transactions on Magnetics, vol. 32, no. 4, pp. 3237-3245 (1996), DOI: 10.1109/20.508387.

- [14] Kwak S.-Y., Kim J.-K., Jung H.-K., Characteristic analysis of multilayer-buried magnet synchronous motor using fixed permeability method, IEEE Transactions on Energy Conversion, vol. 20, no. 3, pp. 549–555 (2005), DOI: 10.1109/TEC.2005.847973.
- [15] Lee K.-D., Lee J., Lee H.-W., *Inductance calculation of flux concentrating permanent magnet motor through nonlinear magnetic equivalent circuit*, IEEE Transactions on Magnetics, vol. 51, no. 11, pp. 1–4 (2015), DOI: 10.1109/TMAG.2015.2438000.
- [16] Wang H.X., Xu X.Z., Feng H.C., Si J.K., Space State Modeling of Permanent Magnet Linear Synchronous Motor and Inductance Parameters Calculation, Applied Mechanics and Materials, vol. 143, pp. 97–102 (2012), DOI: 10.4028/www.scientific.net/AMM.143-144.97.
- [17] Wang H., Feng H., Xu X., Si J., Modeling Analysis and Parameters Calculation of Permanent Magnet Linear Synchronous Motor, J. Comput., vol. 8, no. 2, pp. 463–470 (2013).
- [18] Zhang Y., Ren W., Ji B., Zhong Z., Hao Y., Zhao J., Electromagnetic Performance of Arc-Linear Permanent Magnet Synchronous Motors with Different Slot/Pole Number Combinations, in 2025 7th Asia Energy and Electrical Engineering Symposium (AEEES), IEEE, pp. 334–338 (2025), DOI: 10.1109/AEEES64634.2025.11019054.
- [19] Isfahani A.H., Analytical framework for thrust enhancement in permanent-magnet (PM) linear synchronous motors with segmented PM poles, IEEE Transactions on Magnetics, vol. 46, no. 4, pp. 1116–1122 (2009), DOI: 10.1109/TMAG.2009.2036993.
- [20] Xu X., Li J., Jiang S., Du B., Ji S., Thrust characteristics analysis and parameter optimization of five-phase U-shaped consequent-pole PMSLM, Journal of Electrical Engineering & Technology, vol. 20, no. 1, pp. 575–589 (2025), DOI: 10.1007/s42835-024-01993-7.
- [21] Sun Z., Ding A., Mao Y., Huang C., Xu W., *Improved Adaptive Speed Observer of Permanent Magnet Linear Synchronous Motor with Transient Characteristics*, IEEE Journal of Emerging and Selected Topics in Power Electronics (2025), DOI: 10.1109/JESTPE.2025.3535165.
- [22] Zhang W., Lin G., Huang H., Research on Double Side Linear Synchronous Motor Scheme for High-Speed Propulsion, in 2025 15th International Symposium on Linear Drivers for Industry Applications (LDIA), IEEE, pp. 1–4 (2025), DOI: 10.1109/LDIA64731.2025.11060310.
- [23] Oğuz K., Çift taraflı hava çekirdekli sabit mıknatıslı lineer servo motor tasarımı ve uygulaması, MSc Thesis, Graduate School, Dept. of Electrical and Electronics Eng., Pamukkale Univ., Denizli (2021).
- [24] Chevallier S., Markovic M., Jufer M., Perriard Y., *Linear motor optimization using an analytical model*, Cracow Polland, 5 (2004).
- [25] Gieras J.F., Piech Z.J., Tomczuk B., *Linear synchronous motors: transportation and automation systems*, CRC press (2018).
- [26] Pyrhonen J., Jokinen T., Hrabovcova V., *Design of rotating electrical machines*, John Wiley & Sons (2013).
- [27] Jin J., Zhao H., Xin Y., Sun Y., Simulation and analysis of a PMLSM control system based on SVPWM, in Proceedings of the 29th Chinese Control Conference, IEEE, pp. 3316–3320 (2010).
- [28] Soualmi A., Dubas F., Dépernet D., Randria A., Espanet C., *Inductances estimation in the dq axis for an interior permanent-magnet synchronous machines with distributed windings*, in 2012 XXth International Conference on Electrical Machines, IEEE, pp. 308–314 (2012), DOI: 10.1109/ICEIMach.2012.6349882.
- [29] Ertan H.B., Sahin I., Inductance measurement methods for surface-mount permanent magnet machines, IEEE Transactions on Instrumentation and Measurement, vol. 72, pp. 1–16 (2022), DOI: 10.1109/TIM.2022.3225048.
- [30] Zheng L., Jin J., Investigation of HTS bulk magnet linear synchronous motors, in 2009 International Conference on Applied Superconductivity and Electromagnetic Devices, IEEE, pp. 17–21 (2009), DOI: 10.1109/ASEMD.2009.5306701.
- [31] Fitzgerald A.E., Kingsley C., Umans S.D., Electric machinery, McGraw-Hill Book Company (2003).